Experimental characterization of synchronized interactions between a normal shock-wave and compliant wall

Carmen Riveiro Moreno, Marie Couliou, Nicolò Fabbiane, Olivier Marquet, Reynald Bur

To cite this version:

Carmen Riveiro Moreno, Marie Couliou, Nicolò Fabbiane, Olivier Marquet, Reynald Bur. Experimental characterization of synchronized interactions between a normal shock-wave and compliant wall. ERCOFTAC 2023, Jun 2023, Toulouse, France. ⟨hal-04133176⟩

HAL Id: hal-04133176
https://hal.science/hal-04133176v1

Submitted on 19 Jun 2023

ERCOFTAC Symposium on "Multiphysics critical flow dynamics involving moving/
deformable structures with design applications", Toulouse, France, 7-8-9 June 2023

EXPERIMENTAL CHARACTERIZATION OF SYNCHRONIZED INTERACTIONS BETWEEN A NORMAL SHOCK-WAVE AND COMPLIANT WALL.

C. Riveiro Moreno(1), M. Couliou(1), N. Fabbiane(2), O. Marquet(1) and R. Bur(1)

(1)*DAAA, ONERA, Université Paris Saclay, F-92190 Meudon, France*
(2)*DAAA, ONERA, Université Paris Saclay, F-92322 Châtillon, France*

Abstract.

The interaction of a normal shock-wave (upstream Mach number 1.35) with a compliant wall is characterized experimentally by schlieren visualizations and an optical displacement sensor. Depending on the location of the shock-wave along the compliant wall, three different regimes of interaction are found: large-amplitude synchronized regime, small-amplitude synchronized regime and unsynchronized regime. The large-amplitude synchronized oscillations regime is found for shock locations near 50% of the compliant wall length and the shock presents a lock-in to the second vibration frequency of the structure. The small-amplitude synchronized oscillations regime is found when the shock is located upstream and downstream the middle of the of the compliant wall. In these situations, the shock presents a lock-in to the first and third vibration frequency of the structure respectively. Close to the trailing edge of the compliant wall, the shock oscillation is not synchronized with the compliant wall that oscillates with very small amplitude..

Key words: Fluid structure interaction, Shock/Boundary Layer Interaction, compressible flow.

1. Introduction

Due to minimum weight requirements, the structure of high speed vehicles consists of thin panels or shells-like components that are subjected to large aerodynamic and aerothermal loads caused by supersonic and hypersonic flows. Their reduced thickness and thus flexibility enhance the receptivity of the structure to flow induced vibration which, in case of coupling, can be detrimental to the safety of the vehicle and thus should be taken into account during the design process [16]. The compressible flow around such high speed vehicles is characterized by the presence of shock-waves which interact with the incoming boundary layer, causing large adverse pressure and thermal gradients, as well as unsteady three dimensional separated flow [5]. Hence, better understanding the aeroelastic coupling between shock-waves and flexible walls is fundamental for the design of future high-speed flight vehicles.

Several research groups have conducted experimental campaigns with non intrusive measurement techniques such as Digital Image Correlation (DIC), Pressure Sensitive Paint (PSP) and Particle Image Velocimetry (PIV) among others to describe the fluid-structure interaction. At Imperial College of London, research has focused on the impact the static deformation of the thin panel and the relative position of the shock to it have on the interaction [13, 12, 15, 20, 11]. By varying actuators and cavity pressure, they achieved a panel deformation that recreates the effect of Shock Control Bumps (SCB)[2], thus causing drag reduction and stabilization of the shock unsteadiness. The experimental campaigns conducted in Air Force Research Laboratory (AFRL) Research Cell 19 monitored the influence of thermal stress on the thin panel, cavity pressure, and shock intensity [19, 1]. Brouwer et al. found that in the presence of a weak shock the panel presented limit cycle oscillations, and that these disappear and reemerge as the shock intensity was increased. The impact of temperature has also been studied in DLR at the H2K wind tunnel, where the interaction behaviour was found to be highly sensitive to small changes in temperature [6]. Additionally, it was found that larger incident shock angles prompt the onset flutter when in a non-shock configuration it would not take place. At Florida Center for Advanced Aero-Propulsion, the impact of the compliant wall shape due to change of cavity pressure as well as shock impingement were studied [21]. In the work by Eitner et al. [9], several plate thicknesses were tested. Their results show that the shock oscillates at the first vibration frequency of the panel, being this the first bending mode. Both the panel and the shock-wave present larger oscillations for thinner plates. The tests conducted by A. D'Aguanno [8] present a shock that oscillates at the two first vibration frequencies of the plate, corresponding to the first and third bending modes.

Despite the effort of the research community, the physics behind the coupling between a shock-wave and a compliant wall is still not fully understood. Moreover, most study cases involve an oblique shock caused by either a compression ramp [9] or a shock generator [20, 11, 19, 1, 6, 21]. For normal transonic shocks [13, 12], the interaction has been less explored, and not focused on a strong dynamic coupling scenario. The aim of this study is to shed new light on the fluid structure interaction with the presence of a normal shock-wave (transonic regime). For this purpose, the present work first characterizes the natural unsteady normal shock oscillations over a rigid wall. Knowing its dynamics, a compliant wall is designed so that its natural frequency is of the same order of magnitude as the shock oscillations. Lastly, the fluid structure interaction of the oscillating shock and the compliant wall is studied by high speed schlieren imagery and an optical displacement sensor.

2. Experimental investigation of a shock wave on a rigid wall

2.1 Experimental facility and measurements

Experiments are conducted in S8Ch ONERA's transonic open circuit wind tunnel in Meudon (France), shown in Fig. 1a. This wind tunnel, has been largely used for experimental studies on passive and active (fluidic) control of shock boundary-layer interaction [4]. The stagnation temperature in the settling chamber is 300 ± 10 K and the stagnation pressure 96.0 ± 0.3 kPa.

For this study, the wind tunnel is equipped with a half nozzle that generates an unsteady normal shock-wave with a nominal upstream Mach number of 1.4 [3]. The origin of the cartesian coordinate system (O,x,y) is located at 370 mm from the end of the converging part, as indicated in Fig. 1a, close to the end of the half nozzle. The size of the test section is 100 mm in the wall-normal (y) direction and 120 mm in the spanwise (z) direction. The wind tunnel is equipped with optical accesses on the two lateral doors (white area) and on the top wall of the test section (green area).

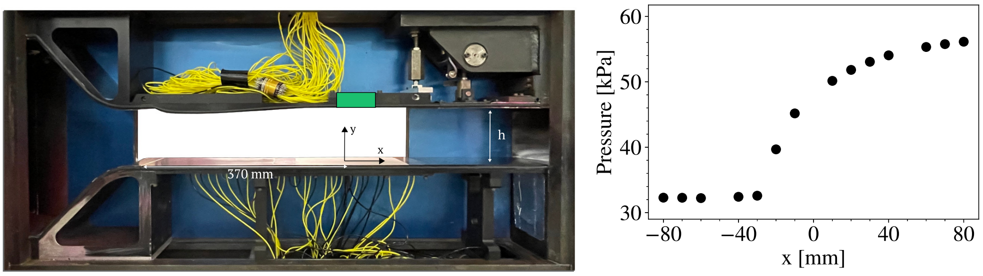

(a) Wind tunnel facility (b) Average pressure distribution

Figure 1: (a) Picture of the high-speed wind tunnel S8Ch showing the cartesian coordinate system (0,x,y) and the optical access for the schlieren visualization (white area) and the wall-tracking (green area). On the top and bottom walls, static pressure probes are installed to retrieve (b) static wall-pressure as a function of the streamwise position x (bottom wall), here for the nominal shock configuration 4 (see table 1).

Case	1	2	3	**4**	5	6	7	8
$\bar{x}_s(mm)$	−45.1	−29.4	−7.3	**−4.8**	32.1	41.1	65.3	73.9

Table 1: Cases investigated in the present study. Average streamwise position of the shock for various heights of the second throat. The nominal case (4) is highlighted in bold.

The flow is “chocked” in the test section by means of a second throat located at the outlet which isolates the test section from downstream perturbations. Varying the height h of the second throat (see Fig. 1a) allows changing the (average) streamwise position $\bar{x}_s$ of the shock in the test section. As the measurement of h is not accurate enough, we only report in Table 1 the shock position for various cases investigated in the present study.

Several measurements are performed to characterize the flow in the nominal shock configuration, number 4 in Tab. 1. The average wall-pressure is measured on the centerline ($z = 0$) of the bottom and top walls using 60 static pressure sensors. Their localisation is illustrated with blue squares in Fig. 2a and typical measurements are shown in Fig. 1b as a function of the streamwise position x, for the nominal configuration. Note that unsteady pressure sensors (Kulite transducers type XCQ-093-15A) are also used to measure the wall-pressure fluctuations at fewer spatial positions on the bottom wall, but results are not reported here. The interested readers are referred to [17] for a discussion about these unsteady pressure measurements. The flow is also analysed by means of schlieren imagery. Schlieren visualizations are conducted with a Z-type Schlieren setup with a high speed Phantom camera and a blue LED source. A vertical knife orientation is used, which yields images whose light intensity is proportional to horizontal density gradients. This orientation enhances the visibility of the shock on the schlieren image. The schlieren videos are acquired at a sampling frequency of 7 kHz for a duration of 3.87 s, which used the maximum camera memory capacity.

The schlieren images are used to track the location of the shock as shown in Fig. 2a. This was conducted on the normal part of the shock-wave (Fig. 2a, white rectangle).

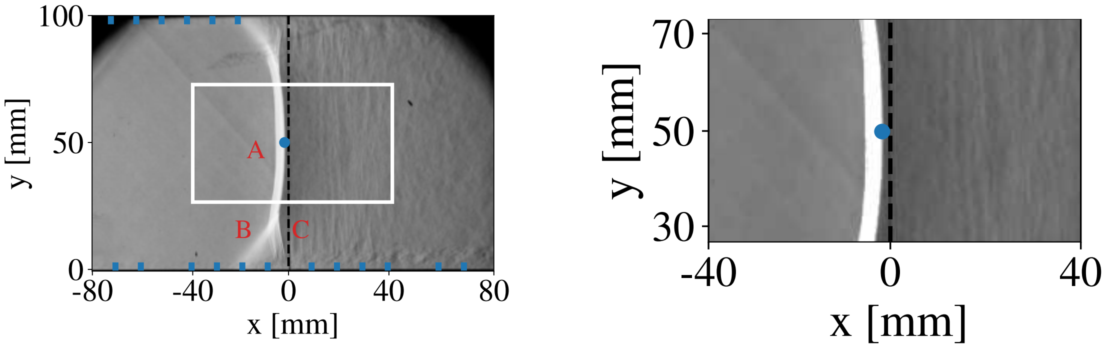

(a) Instantaneous schlieren images

(b) Zoom on schlieren image (a)

Figure 2: (a) Full view of an instantaneous schlieren image with (A) the normal shock and (B,C) the front and rear legs of λ-shaped shock-foot. The blue squares correspond to the localisation of static pressure sensors. The white rectangle delimits (b) the close-up view around the normal shock. The dot corresponds to a particular tracked position $x_s(t)$ of the normal shock in the symmetry plane $y = 50$ mm of the test section. Nominal shock configuration 4 (see table 1).

Therefore, for each snapshot, the region displaying the upper and lower shock feet is cut out of the images (Fig. 2b). The schlieren images are reported in grey scale, where an intensity value of 255 corresponds to white and 0 to black. In order to increase the brightness of the shock, all pixels whose intensity are above 180 in the grey scale are set to 255 (white) (Fig. 2b). For each y location, the location in x of the most downstream pixel whose intensity is 255 (white) is recorded. As a result, one obtains the temporal displacement of the shock for each y location on the normal shock. As similar displacement signals are retrieved for different locations along y, the middle position $y = 50$ mm will be used to represent the motion of the shock in this study (Fig. 2, blue dot).

2.2 Description of the nominal rigid configuration

We now detail the nominal configuration denoted 4, highlighted in bold in the table 1. The Mach number upstream of the shock is equal to 1.35. Fig. 1b shows the pressure along the lower wall of the test section for this configuration. This pressure distribution reveals the high adverse pressure gradient the normal shock imposes on the flow. At the shock location $\bar{x}_s(mm) = -4.8$, no pressure plateau is visible meaning that the shock does not induce a massive separation or recirculating flow.
The schlieren image in Fig. 2a presents an instantaneous image of the flow in a zoom region around the shock. In it, it is possible to observe a normal shock (A) with its λ shaped shock foot, with the front leg (B) composed of a compression fan, and the rear leg (C) consisting of an oblique shock. The existence of a λ region confirms the presence of shock induced separation, although, for this configuration, it is small. Note that the apparent thickness of the shock is due to a spanwise integration of light.
In order to study the dynamics of the shock, x_s, the location in x of a point at the shock at $y = 50$ mm (Fig. 2a, blue dot) was tracked in time. The fluctuating part, $x_s^{'} = x_s - \bar{x}_s$, of the resulting signal is presented in Fig. 3a (grey). For the

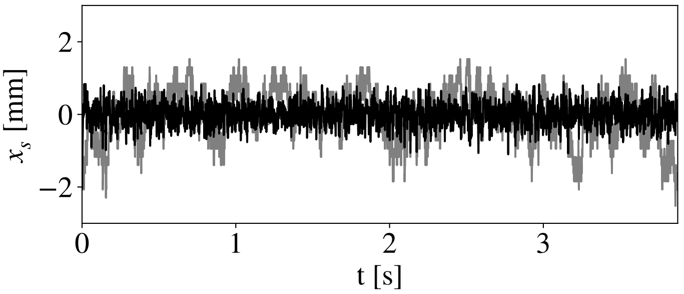

(a) Shock displacement signal

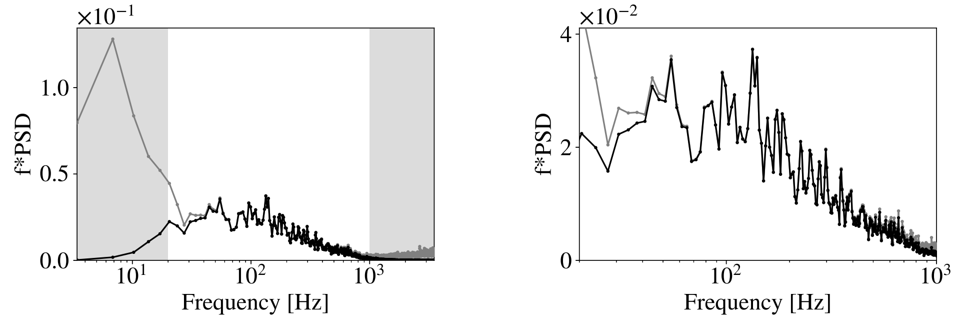

(b) f*PSD Shock displacement

(c) f*PSD Shock displacement zoom

Figure 3: Nominal configuration 4. (a) Fluctuation of the streamwise displacement of the shock $x_s' = x_s - \bar{x}_s$ as a function of time, defined by substracting the average position from the instantaneous displacement x_s obtained by tracking the shock position in the instantaneous schlieren. (b-c) Power spectral density (premultiplied by the frequency) as a function of the frequency for the shock displacement signal shown in (a). The grey areas in (b) correspond to spurious oscillations as explained in the text. (c) Zoom in the frequency range of interest. In grey the raw signal, in black the filtered signal as explained in the text.

computation of the power spectrum density using the Welch method, 2048 samples per block were used with 50% overlap. The premultiplied spectrum of the shock displacement signal is presented in Fig. 3b (grey). The low frequency peak present in the spectrum, below 20 Hz, is generated by fluctuations of the stagnation pressure in the settling chamber. These fluctuations were found to be related to vibrations of the wind tunnel installation. On the other hand, the high frequency content, above 1kHz, is due to noise steaming from the tracking method to retrieve the shock location. Thus, the spectrum of the natural unsteady shock oscillation corresponds to the non shaded area in Fig. 3b (grey). Fig. 3b presents a zoom of the spectrum in this area. As it can be seen, the shock oscillations are low frequency and broadband in nature, in agreement with results reported in literature [18, 10, 7, 5]. For the present study, the low frequency bump is centered around 100 Hz.

In order to understand the contribution of the natural shock oscillations to the total shock displacement signal, the signal was filtered with a Butterworth filter of order 2, a low pass at 20 Hz and a high pass at 1000 Hz. The resulting signal is presented in Fig. 3a and the spectrum in Fig. 3b-c (black). As it can be seen in the spectrum, within the frequency range of interest (Fig. 3b-c), the filtered spectrum matches that of the raw data, whereas the forcing from the settling chamber and the spurious oscillations have been removed. Hence, the oscillations present in the

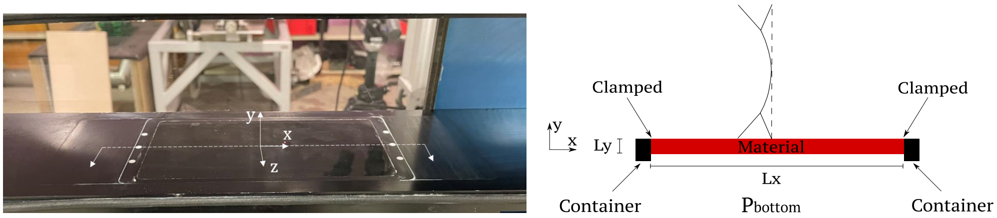

(a) Lower wall test section
(b) Sketch of compliant wall setup

Figure 4: (a) View of the compliant wall on the lower wall of the test section. (b) Sketch of a lateral view along the center line (white dashed line on (a)) of the compliant wall with the location of the shock.

filtered signal in Fig. 3a (black), correspond to the oscillations steaming from the interaction of the shock with the incoming boundary layer.
Since the forcing from the settling chamber and the spurious noise coming from the shock tracking method are not within the frequency range of the natural shock oscillations (Fig. 3b-c), there is no need to filter the shock displacement signal. For a better comprehension, all the shock displacement spectra will be presented only from 20 Hz to 1000 Hz in this study.

3. Investigation of the shock-wave/compliant-wall interaction

3.1 Description of the compliant wall

The compliant wall is made of a polyurethane block that is inserted in an aluminum container. The streamwise (x) and spanwise (z) lengths of this container are respectively fixed to 160 and 85 mm, the latter being constrained by the spanwise length of the test section (120 mm). The thickness (y) of this container may be varied but will be fixed in the present study to 20 mm. As shown later, this thickness allows the lowest natural vibration modes of the compliant wall to be in the range of frequency $30Hz \leq f \leq 200Hz$ characterizing the shock oscillation. As shown in Fig. 4a, the container is placed on the lower wall of the test section. Its midpoint in the streamwise direction coincides with the origin of the cartesian coordinate system, i.e. $x = 0$. Therefore, for the nominal configuration (denoted 4) described before, the shock is almost located at the center of the compliant wall, as sketched in Fig. 4b. The polyurethane block is clamped to the four lateral surfaces of the container but is free to move at the bottom and top surfaces. The top surface is the interface with the flow and the pressure distribution therefore depends on the shock position. Under the bottom surface, the pressure is constant but not necessarily equal to the atmospheric pressure (leaks, gaps, ...). Its value is measured using a pressure probe so as to obtain the pressure difference between the top and bottom surface, and it was found to be equal to the average pressure on the test section.

3.2 Optical measurements of the wall displacement

The vertical displacement of the compliant wall in the symmetry plane ($z = 0$) of the test section is measured using two non-intrusive optical methods.

The first method is based on the schlieren images. As the compliant wall deforms upwards, it blocks the light projecting a shadow which translates into a black area on the schlieren image (Fig. 5a). Since the schlieren method provides a spanwise integration of light, this deformation, corresponds to the highest displacement of the material, which is found at the centerline ($z = 0$). Thus, the schlieren images provide access to the compliant wall's deformation at $z = 0$. For this purpose, the width of the images matches the length of the compliant wall.

The first step to extract this data from the schlieren images is to crop the image so that only the lower test section wall and the lower shock foot are displayed. Then, a Sobel filter that computes the pixel intensity gradient on the y direction is applied to retrieve horizontal edges on the image, and thus the compliant wall edge. The resulting image, in grey scale, will display the edge of the compliant wall in black. Then, for each x position, the location of the compliant wall edge in y, pixel intensity equal to 0 (black), is retrieved. When this procedure is conducted on all the schlieren images, one obtains the temporal evolution of the compliant wall's displacement along x.

The videos are sampled at 7 kHz for a duration of 3.87 s. Vertical knife orientation is used so that horizontal density gradients are retrieved in order to enhance the visibility of the shock, which helps the tracking of the shock location as explained in §2.1. This knife orientation has also the advantage that it does not highlight the boundary layer, which would interfere with the wall tracking process.

Nonetheless, this technique presents two disadvantages. Firstly, the lateral windows of the wind tunnel only allow optical access to the test section, meaning that any downward motion of the compliant wall is not captured (Fig. 5b). Secondly, the resolution of the displacement is linked to the image resolution in pixels, which for this study is 0.22 mm/pixel, which is troublesome when small displacements are at play.

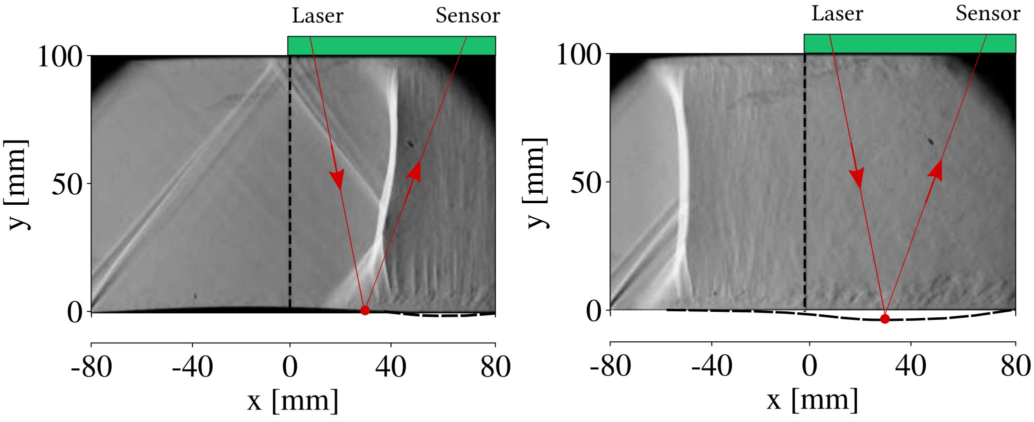

(a) Case 6.

(b) Case 1.

Figure 5: Sketch of the two optical techniques used to measure the wall displacement illustrated with cases (a) 6 and (b) 1. The dashed black line indicates $y < 0$ wall displacement that cannot be observed with schlieren. Green rectangles show the location of the optical access (on the upper wall of the test) for the light beam (red line) allowing us to measure the displacement of one point (red dot) on the compliant wall.

Another way the compliant wall's displacement was measured was through a non-intrusive optical pointwise displacement sensor Keyence LK-G402. The resolution of this sensor is 0.2 μm, much higher than the one provided by the schlieren. The measurements were conducted through the optical access on the test section (Fig. 5, green rectangle), which allows downward displacement measurements (Fig. 5b), not available with the schlieren setup.

The sensor was mounted on a metallic structure outside of the wind tunnel facing the wind tunnel's upper wall, which is also equipped with a window. The sensor points at location x_{sensor} = 27 mm and z_{sensor} = 2 mm (Fig. 5, red dot). Due to restrictions on the optical window of the test section, it was not possible to install the sensor perpendicular to the compliant wall. Therefore the measured displacement is not along the y axis. Additionally, owing to reflection issues, data was not available for shock configurations 3 and 4. Nonetheless, for the reminding configurations, its average value can still be used qualitatively, and this does not entail any problem for the dynamic analysis of the compliant wall's motion. The signal for all shock configurations was acquired at 20 kHz and 60 s.

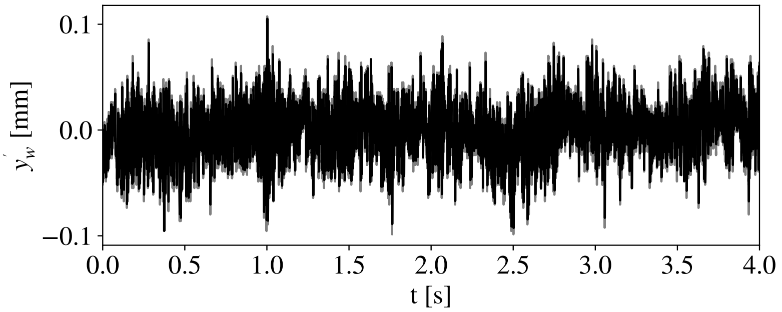

(a) Displacement signal of the wall from the displacement sensor

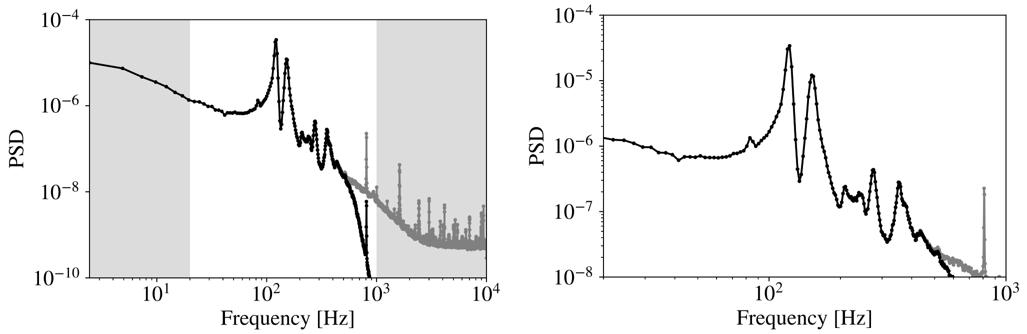

(b) PSD of the wall displacement (c) Zoom on PSD of the wall displacement

Figure 6: Fluctuating part of the compliant wall displacement signal $x_s^{'} = x_s - \bar{x}_s$ and its power spectrum density (PSD). In grey the raw data, in black the filtered data. Grey area in (b) referrers to the range of frequencies with spurious data on the shock displacement spectrum shown in Fig. 3b

Fig. 6a presents an interval of 4 s of the total duration of the displacement fluctuation signal, $x_s^{'} = x_s - \bar{x}_s$, measured with the optical sensor for configuration 7. The signal (grey) is superimposed with the filtered signal (black) which will be later explained. The amplitude of the oscillations is less than 0.1 mm, meaning that these fluctuations would not be captured by the schlieren images as their resolution is 0.22 mm per pixel. The power spectrum density of the entire signal is presented in Fig. 6b (grey), and was obtained through the Welch method using 8192 samples per block and 50% overlap.

The grey areas presented in the spectrum in Fig. 6b, refer to the frequency range where spurious data has been found on the shock displacement spectrum on the rigid configuration (Fig. 3b). The spectrum of the wall displacement, presents no peaks below 20 Hz (grey area on the left), meaning that the low frequency forcing of the flow coming from the settling chamber (presented in §2.1), does not interact with the compliant wall. The same result was found in all configurations. On the grey area on the right, starting at 1000 Hz, there are frequency peaks, related though to electronic noise. This implies that also in the compliant wall dynamics, high frequency content on the spectrum is spurious.

So as to mitigate the effect of the non-physical peaks, a high pass 6th order Butterworth filter at 600 Hz was applied to the displacement signal. The parameters of the Butterworth filter were chosen to include in the attenuation the first non-physical peak found already at 800 Hz. The resulting filtered signal and spectrum are represented in Fig. 6 in black. As shown in Fig. 6a the filtered (black) and raw (grey) signals are coincident, meaning that the contribution of the high frequency noise to the displacement signal is barely relevant. Fig. 6c presents a zoom on the frequency range of interest, where it is possible to observe frequency peaks that correspond to the different vibration frequencies of the compliant wall. For a better interpretation, the different displacement spectra presented in this study are filtered with the aforementioned Butterworth filter and displayed from 20 Hz to 1000 Hz to allow a comparison with the shock displacement spectrum.

Clearly, the experimental measurements are too sparse to allow a complete description of the wall deformation. Therefore, we will propose in §3.4 a method to reconstruct the instantaneous displacement by combining a numerical model of the wall displacement with the experimental data. The numerical modeling is detailed in the next section.

3.3 Experimental and numerical characterisation of the compliant wall's displacement

The mechanical properties of polyurethane were characterised with shear torsion tests on a rheometer at Laboratoire de Mécanique des Solides at École Polytechnique. This provided the evolution of the complex shear modulus $G^* = G' + iG''$ as a function of frequency for the temperature expected at the surface of the wind tunnel. For the frequency range of the shock oscillations, the real part of the shear modulus, G', is practically constant and equal to 1.0095 MPa. Using the Lamé coefficients and taking into account the correspondence principle of viscoelasticity, the Young storage modulus E' can be deduced from the shear storage modulus G'. This yields a Young Modulus E' equal to 3.03 MPa. The density of the material was found to be $\rho_s \sim 1000 kg/m^3$.

To validate this value, we propose to compare the static deformations measured experimentally and predicted numerically. For the experiments, it is advantageous to consider configuration 8 where the shock position ($\bar{x} = 73.9$ mm) is closer to the downstream side of the compliant wall ($x = 80$ mm). Indeed, the wall-normal displacement of the compliant wall is upward ($y_w > 0$) for most of the streamwise positions and can thus be captured with schlieren vizualisations. The time-averaged wall-normal displacement of the compliant wall is shown in Fig. 7b with the solid curve in red. The maximal displacement is around 2 mm, i.e. 10 times smaller than the thickness of the material and is obtained around the middle point of the compliant wall $x \sim 0$. For $x > 60$ mm, the wall displacement is downward ($y_w < 0$) and thus not observable in the schlieren vizualisation. The red dot seen in Fig. 7b corresponds to the time-averaged displacement obtained from instantaneous pointwise measurements with the non-intrusive laser technique at the single point $x_{sensor} = 27$ mm. The two techniques used to measure the wall displacement thus give coherent results although they do not perfectly match.

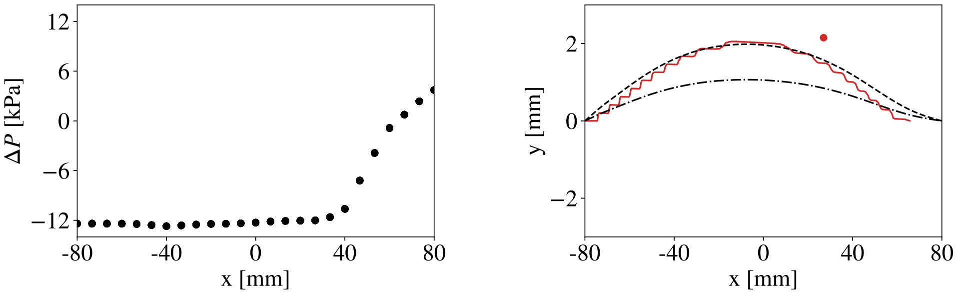

(a) Pressure difference distribution

(b) Compliant wall deformation

Figure 7: Configuration 8 corresponding to the shock position $\bar{x} = 73.9$ mm. (a) Averaged wall-pressure difference, $\Delta P(x) = P(x) - P_{bottom}$, where $P(x)$ is measured on the rigid wall as a function of the streamwise coordinate x. (b) Wall-normal displacement y_w of the compliant wall as a function of x. The solid red curve corresponds to the time-averaged displacement extracted from the schlieren vizualisation. The dashed and dashed-dotted curves are numerical predictions of the static displacement computed using the experimental wall-pressure as static aerodynamic loading at the interface for the Young modulus $E = 3.03$ MPa (dashed-dotted) and $E = 1.63$ MPa (dashed). The red dot is the average-displacement measured with the optical pointwise sensor.

The wall-normal static displacement of the compliant wall can also be estimated numerically as described in §A using the static aerodynamic wall-pressure difference, $\Delta P(x) = P(x) - P_{bottom}$, where $P(x)$ is measured on the rigid wall and P_{bottom} with a static pressure probe in the cavity. Fig. 7a presents the wall pressure difference for case 8. Compared to the nominal case (4, shown in Fig. 1b), the sharp streamwise variation of the pressure associated with the shock is located more upstream. In the present case, the pressure upstream of the shock is lower than the pressure measured under the compliant wall, and thus the pressure difference is negative. More specifically, for $x < 60$ mm, the pressure difference between the top and bottom interface induces an upward aerodynamic loading, while for $x > 60$ mm, a downward aerodynamic loading is applied. The numerical prediction of the static displacement induced by such aerodynamic loading is shown in Fig. 7b for the centerline $z = 0$. For the Young modulus $E = 3.03$ MPa measured with the rheometer, we obtain the displacement displayed with the dash-dotted curve. It clearly underestimates by a factor of 1.86 the displacement measured experimentally (solid curve red). By adjusting the value to $E = 1.63$ MPa, we obtain (dashed curve) a much better agreement with the experimental result. Therefore, we propose in the following to estimate the Young modulus of our material as $E = 1.63$ MPa.

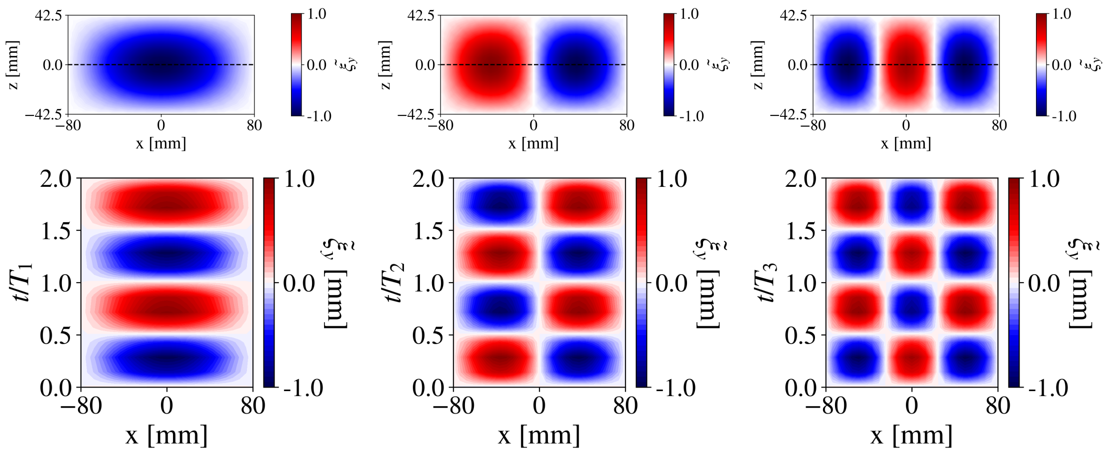

(a) $f_1^n = 104.3$ Hz (b) $f_2^n = 133.2$ Hz (c) $f_3^n = 179$ Hz

Figure 8: Natural vibration modes of the structure (polyurethane inserted in the aluminium container) for the three lowest frequencies. Wall-normal displacement of the compliant wall (fluid/solid interface) shown (top) in the two-dimensional plane (x, z) at a given instant and (bottom) shown in the spatio-temporal diagram for the centerline $z = 0$

.

The dynamic of the compliant wall can also be estimated numerically by examining the natural vibration modes of the structures as described in §A. The wall-normal displacement of the top interface (compliant wall) is shown in Fig. 8 for the three eigenmodes corresponding to the lowest frequencies. The instantaneous displacements in the two-dimensional plane (x, z) are displayed in the top figures while the temporal evolution of the displacement at the centerline of the test section $z = 0$ is shown in the bottom figures. The first mode is characterized by maximal/minimal displacements at the center, i.e. $(x, z) = (0, 0)$, oscillating at frequency $f_1^n = 104.3$ Hz. The second and third modes display a spatial oscillation in the streamwise direction. The second mode, oscillating at frequency $f_2^n = 133.2$ Hz, is characterized by one node (zero displacement) at the center of the compliant wall and maximal/minimal displacements in the centerline at $x = \pm 40$ mm. The third mode, oscillating at frequency $f_3^n = 179$Hz, is characterized by two nodes located at $x = \pm 27$ mm with maximal/minimal displacements in the centerline at $z = \pm 53$ mm.
The natural frequencies of the first two modes are close to the range of frequency characterizing the oscillation of the shock on the rigid wall, as shown in Fig. 3b.

3.4 Reconstruction of the instantaneous wall displacement

For most cases investigated here, the downward displacement of the wall prevents extracting its positions from schlieren images. In these cases, the optical sensor gives access to only a pointwise measurement of the wall. To complete these experimental data, we propose to reconstruct the full displacement of the compliant wall as follow. This reconstruction method is based on the three dimensional linear equation model used to describe the behaviour of the material and it is presented in §A.

The instantaneous vertical displacement of the interface at the centerline $z = 0$, denoted $y_w(x,t)$, is modeled as the sum of a static component and a fluctuating component, i.e.

$$y_w(x,t) = a_0\, y_w^0(x) + \sum_{k=1}^{N} \left(a_k^c\, \hat{y}_{w,r}^k(x)\, \cos(2\pi f_k t) + a_k^s\, \hat{y}_{w,i}^k(x)\, \sin(2\pi f_k t) \right). \qquad (1)$$

The first term is the static component with a constant amplitude a_0 and a spatial shape $y_w^0(x)$. These amplitudes and shape can be estimated using the static numerical computation described before. Knowing the spatial shape, the amplitude can also be retrieved with the method described below. The second term in the above decomposition is the fluctuating component that is expanded as a Fourier series. The real coefficients a_k^c and a_k^s are the amplitudes of the modes vibrating at the frequency f_k. The spatial shapes $\hat{y}_{w,r}^k$ and $\hat{y}_{w,i}^k$ are defined as the real and imaginary parts of the vertical component of the natural vibration mode

$$\hat{y}_w^k(x) = \left(\boldsymbol{\xi}_n^k\right)_y (x, y=0, z=0) \qquad (2)$$

restricted to the centerline ($z = 0$) of the fluid/solid interface ($y = 0$). These natural vibration modes are eigenvectors from the eigenvalue problem 13 shown in §A and are associated with natural vibration frequencies $f_k^n = \omega_k^n / 2\pi$, ω_k^n being the square root of the corresponding eigenvalue. Note that in the proposed model (1), the modes rather vibrate at frequencies f_k determined via a frequency analysis of the experimental wall-displacement signal: the identified peaks in frequency are associated to each mode in order of appearance. Indeed, in the coupled fluid-structure system, the structure does not necessarily oscillate at its natural frequencies and frequency-shift usually appears because of the coupling with the fluid, thus the need to identify the correct frequencies from the experimental data.

The coefficients a_k^c and a_k^s are computed by means of a least-square fit of the experimental data. The data may come from the tracking of the wall position in the schlieren images or from the optical displacement sensor. The former is used when the deformed wall is visible in the schlieren image and the oscillation amplitude is significantly larger than the image resolution. In this case, the set of observations used to fit the model is defined as

$$\mathcal{O}_{schlieren} = \{(x_i, t_j)_{1 \le i \le N_x, 1 \le j \le N_t} \mid y_w^{exp}(x_i, t_j) > \epsilon\} \qquad (3)$$

where N_x is the number of points (pixels) in a schlieren image and N_t is the number of images. The positive real number ϵ is introduced to select wall-position visible in the image while accounting to the image resolution. As shown in §3.2, the schlieren resolution is 0.22 mm. Therefore, for the computation ϵ is set to 0.22 mm. The total number of observations used for the reconstruction is $N_{schlieren} = N_t \times N_x = 704 \times 1000 = 704000$; the number of retained points in $\mathcal{O}_{schlieren}$ is 227378.

On the other hand, the displacement sensor is able to measure the complete oscillation dynamic but only for one spatial location. The set of observations used for fitting the model is then defined as

$$\mathcal{O}_{sensor} = \{(t_j)_{1 \le j \le N_{sensor}} \mid y_w^{exp}(x_{sensor}, t_j)\} \qquad (4)$$

where $N_{sensor} = 600000$ is the number of temporal measurements obtained with the optical displacement sensor at point $x_{sensor} = 27$ mm.

The model is then fitted to the observations. To that aim, we classically write that the wall-displacement model (1) is equal to the available measurements, for instance

$$y_w^{exp}(x_i,t_j) = a_0\, y_w^0(x_i) + \sum_{k=1}^{N} \left(a_k^c\, \hat{y}_{w,r}^k(x_i)\, \cos(2\pi f_k t_j) + a_k^s\, \hat{y}_{w,i}^k(x_i)\, \sin(2\pi f_k t_j) \right)$$

for any points in the schlieren data-set $\mathcal{O}_{schlieren}$. This relation can be recast as a linear problem

$$\boldsymbol{y}_w^{exp} = \boldsymbol{\Upsilon}\boldsymbol{a} \tag{5}$$

where $\boldsymbol{y}_w^{exp} = \left(y_w^{exp}(x_1,t_1),\cdots,y_w^{exp}(x_{N_x},t_{N_t})\right)^T$ is a vector gathering experimental observations, $\boldsymbol{a} = \left(a_0, a_1^c, a_1^s, \cdots, a_N^c, a_N^s\right)^T$ is the vector gathering unknown amplitudes of model and $\boldsymbol{\Upsilon}$ is the interpolation matrix defined as

$$\boldsymbol{\Upsilon} = \begin{bmatrix} \vdots & & \vdots & \vdots & \\ y_w^0(x_i) & \dots & \hat{y}_{w,r}^k(x_i)\cos(2\pi f_k t_j) & \hat{y}_{w,i}^k(x_i)\sin(2\pi f_k t_j) & \dots \\ \vdots & & \vdots & \vdots & \end{bmatrix} \tag{6}$$

This linear system is overdetermined since the number of equations (rows of $\boldsymbol{\Upsilon}$) is larger than the number of unknowns (coefficients of $\boldsymbol{a}$). Still, it is possible to solve this type of system by means of a least-square approach. Left-multiplying (5) with the transpose of the interpolation matrix, we obtain

$$\boldsymbol{\Upsilon}^T\boldsymbol{\Upsilon}\boldsymbol{a} = \boldsymbol{\Upsilon}^T\boldsymbol{y}_w^{exp} \tag{7}$$

where $\boldsymbol{\Upsilon}^T\boldsymbol{\Upsilon}$ is a square matrix of small dimension, equal to the number of unknowns. It can be inverted, yielding

$$\boldsymbol{a} = \underbrace{\left(\boldsymbol{\Upsilon}^T\boldsymbol{\Upsilon}\right)^{-1}\boldsymbol{\Upsilon}^T}_{\boldsymbol{\Upsilon}^\dagger}\ \boldsymbol{y}_w^{exp} \tag{8}$$

where $\boldsymbol{\Upsilon}^\dagger$ is known as the Moore-Penrose pseudo-inverse. From a computational point of view, the pseudo-inverse is computed via the Python library `scipy`, which implements a method based on the singular-value decomposition of the matrix.

An example of the reconstruction from wall-tracking data coming from the schlieren images is presented in Fig. 9a-b. This corresponds to the shock configuration 4. Fig. 9a shows the comparison between the reconstructed displacement signal (dashed lines) and the experimental one (solid lines) extracted at the wall streamwise location $x = -43$ mm. We recall that the data set used for fitting the model is not limited to this temporal signal, as explained before, but includes all positive instantaneous positions. The signal is periodic and the wall is not visible ($y_w < 0$) in part of the period. Clearly, the algorithm allows us to reconstruct the complete signal. The vibration frequency f_k of the first three modes used for the reconstruction and their associated amplitudes $a_k = \sqrt{({a_k^s}^2 + {a_k^c}^2)}$ are given in Tab. 2. Being a_2 the highest values, it is clear that the second mode vibrating at frequency $f_2 = 153$Hz is the dominant one. This is also shown in Fig. 9b that compares the spectra of the

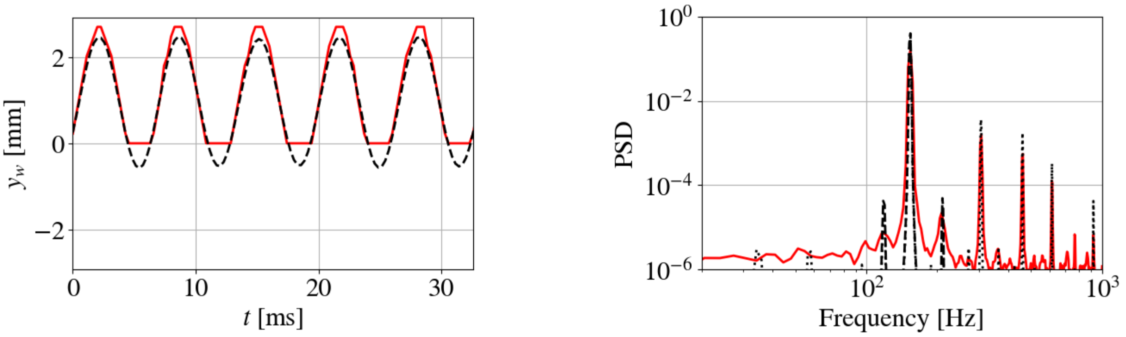

(a) Case 4: time signals at $x = -43\,\mathrm{mm}$.

(b) Case 4: spectra at $x = -43\,\mathrm{mm}$.

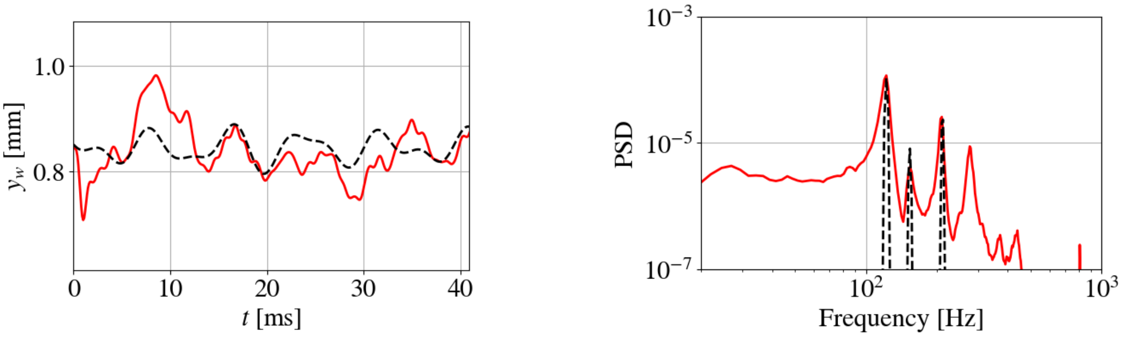

(c) Case 6: time signals at $x = 27\,\mathrm{mm}$

(d) Case 6: spectra at $x = 27\,\mathrm{mm}$.

Figure 9: Wall-displacement reconstruction from wall-tracking data (Cases 4 and 6 in Tables 1-2). (a, c) Temporal signals at two streamwise positions. Solid and dashed lines correspond to experimental and reconstructed data, respectively. (b, d) Power Spectral Density as a function of frequency for the experimental (solid), reconstructed (dashed). The clipped reconstructed signal (dotted) is also reported in (b); see text for description.

experimental (solid) and reconstructed (dashed) wall displacement signal (Fig. 9a). Note that in the experimental spectrum, we also observe peaks that are multiples of the leading frequencies f_2. These are spurious peaks appearing in the spectrum because the experimental signal is clipped when $y_w < 0$, and thus are not used in the reconstruction. This effect can be easily shown by clipping the reconstructed signal when $y_w < 0$. The frequency spectrum of this synthetic signal is shown with the dotted line in Fig. 9b. Super-harmonic peaks appear while they do not exist in the original spectrum (dashed).

Fig. 9c-d reports also an example of reconstruction from data measured with the optical displacement sensor at point $x_{sensor} = 27\,\mathrm{mm}$ for the shock configuration 6 (Tab. 1). In this case, we recall that the data set is much more limited since only the temporal signal at this point is used to fit the model. Fig. 9c compares the reconstructed displacement signal (dashed line) with the experimental one (solid line). Even if the time evolution is not perfectly recovered, the spectral content at the identified frequency peaks is more than satisfactory (Fig. 9d). As in the previous example, further information that is retrieved by this analysis is the dominant mode-shape of the structure. This case is of particular interest since it highlights how a single-point measurement can be misleading: if the signal spectrum identifies $\hat{y}_w^1$ as

Case	f_1 [Hz]	a_1 [mm]	f_2 [Hz]	a_2 [mm]	f_3 [Hz]	a_3 [mm]	Data source
1	**119**	**0.060**	149	0.016	205	0.011	displ. sensor
4	119	0.019	**153**	**1.554**	208	0.025	wall-tracking
6	122	0.034	151	0.009	**210**	**0.085**	displ. sensor

Table 2: Frequencies and reconstructed modal amplitudes (cf. Table 1 for case definition). The amplitudes a_k are defined as $\sqrt{{a_k^s}^2 + {a_k^c}^2}$, cf. (1). For each case, the modal shape associated with the largest amplitude is reported in bold.

the dominant mode at $f_1 = 119\,\text{Hz}$, the true dominant mode is $\hat{y}_w^3$ at $f_3 = 210\,\text{Hz}$ (Tab. 2). This is due to the fact that the displacement sensor is close to a node of $\hat{y}_w^3$ (Fig 8c). The amplitude a_k of a basis $\hat{y}_w^k$ vibrating at f_k is linked to the wall displacement amplitude $Y(f_k, x)$ at a given streamwise position x by the relation

$$|Y(f_k, x)| = a_k\,|\hat{y}_w^k(x)|.$$

If x is positioned close to a node of $\hat{y}_w^k$ – i.e. $\hat{y}_w^k(x) \approx 0$ –, the apparent amplitude of the mode at this location will be biased. The algorithm is able to overcome this limitation by retrieving the real modal amplitudes a_k and, thus, identifying the true dominant mode.

Tab. 2 presents the modal amplitudes for a selection of the shock cases presented in this work. These cases are representative of the different shock oscillation regimes observed in the experimental data and that will be discussed in the following.

3.5 Description of various regimes of interaction.

Different regimes of interaction between the compliant wall and the shock wave are found depending on the shock position. First, we describe a regime of large-amplitude synchronized interaction where the amplitude of wall's vibration is of the same order as its static deviation. Then we focus on two regimes of small-amplitude synchronized interaction where the wall's vibration is of lower amplitude than its static deviation. A last regime exhibiting no synchronization between the wall and shock dynamics is described before classifying all of these regimes as a function of the shock positions.

Regime of large-amplitude synchronized interaction To illustrate this regime of interaction characterized by large periodic synchronized oscillations of the compliant wall and the shock, we describe the results obtained for the shock configuration 4 for which the normal shock is located around $\bar{x}_s = -4.8$ mm as shown in Tab.1.

Fig. 10a shows the frequency spectrum of the wall-displacement at $x = -36.9$ mm, located upstream of the shock. At this point the maximum upward deformation takes place. The spectrum shows a dominant peak f_2 at 153 Hz as well as two other minor peaks f_1 and f_3, located at 119 Hz and 205 Hz (dashed lines). The frequency peaks above 205 Hz are multiples of the leading frequency f_2, 153 Hz. These are the result of the lack of displacement information when $y_w < 0$ as illustrated in §3.4. The three frequencies identified experimentally are close to the natural frequencies of the material ($f_1^n = 104.3$ Hz, $f_2^n = 133.2$ Hz, $f_3^n = 179$ Hz) determined numerically in §3.3.

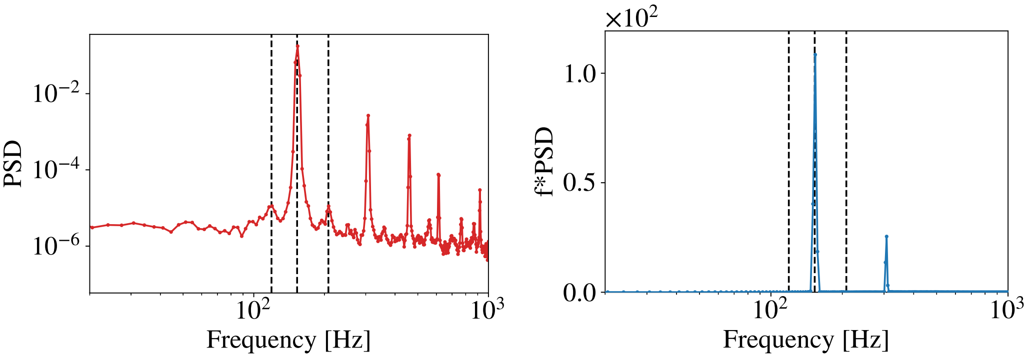

(a) PSD of compliant wall displacement (b) f*PSD shock displacement

Figure 10: Regime of large-amplitude synchronized interaction illustrated with the shock position 4. (a) Power spectrum density of the wall-displacement extracted from schlieren images at point $x = -36.9$ mm and (b) premultiplied power spectrum density of the shock-displacement tracked in the schlieren images. Dashed lines correspond to the first vibration frequencies of the compliant wall.

The spectrum of the shock displacement obtained at the center of the channel is presented in Fig. 10b. The dashed lines indicate the three vibration frequencies of the structure. Just as for the compliant wall, the flow spectrum is dominated by a peak at 153 Hz, accompanied by its first harmonic $2f$. Therefore, both the structure and the flow present large synchronized periodic oscillations at the same frequency $f_2 = 153$ Hz, which is the second vibration frequency of the structure. This large-amplitude peak at a frequency characteristic of the compliant wall clearly suggests a lock-in of the shock oscillation with the second vibration mode of the structure. In this regime of interaction, the frequency spectrum of the shock-displacement is notably different from the rigid wall case, which is characterized by a broadband amplification of frequencies with much weaker amplitudes (see Fig. 3c).

To further explore the interaction, the temporal evolution is shown in Fig. 11 by depicting instantaneous schlieren images for six different instants along a full oscillation cycle of period $T = 1/f = 6.5$ ms. The blue dots show the positions of the shock in the center of the channel, while the red (resp. green) dots highlight the position of the compliant wall upstream (resp. downstream) of the shock at $x = -40$ mm (resp. $x = 40$ mm). At the initial time t_0 of the oscillation period (Fig. 11a), an upward displacement of the wall is clearly visible for -80 mm $\leq x \leq 0$ mm with a maximum located around $x = -40$ mm. This is the maximum upward deformation of the compliant wall during the cycle. At this instant, the shock at the channel's center is located at $x = 0$ mm and presents a large λ shape on the lower foot. The front leg is located slightly downstream of the position of the maximal deformation. Downstream, a large separation region may occur and large structures are shed in the mixing layer. At the time $t_1 = t_0 + T/6$ (Fig. 11b), the upward deformation of the wall decreases while the shock moves upstream. At the time $t_2 = t_0 + 2T/6$, we do not see any upward deformation of the wall and the shock has continued to move upstream. Regarding the shock, the λ region has decreased, indicating a reduction in the separation under the shock foot. Likewise, there is a reduction in the size of the structures shed downstream of the shock foot. At the time $t_3 = t_0 + T/2$ corresponding to half-period of the cycle, there is no visible displacement of the compliant wall upstream of the shock, but an upward deformation is observed downstream of the shock with a maximum of around 40 mm. Note that this upward displacement is weaker downstream the shock than upstream the shock (compare with Fig. 11a). In the meantime (from t_2 to t_3), the streamwise position of the shock has barely changed but the size of the λ region is reduced and the shedding of the structures appears less intense. At time $t_4 = t_0 + 4T/6$, no upward deformation of the wall is visible downstream of the shock, while a very small deformation is visible upstream of the shock. The shock has moved downstream and its topology resembles the one found in the rigid case (Fig. 2a). Finally, at the last time of the cycle $t_5 = t_0 + 5T/6$, the upward deformation of the compliant wall is more pronounced upstream of the shock. This upward motion is accompanied by a downstream displacement of the shock. The features here observed resemble those present in t_0.

In order to give an overall view of the compliant wall displacement, Fig. 12a shows isocontours of the vertical displacement in a spatio-temporal diagramm where x is the streamwise position and t/T is the time normalized by the oscillation period T. Since downward displacements of the wall are not visible in the schlieren images, negative values are not visible in this figure and are displayed here with grey color. The various instants of the schlieren images shown in Fig. 11 are marked here with horizontal dashed lines. This spatio-temporal evolution clearly confirms that the upward displacement of the compliant wall is of larger magnitude upstream of the shock, the position of the latter being shown with the black curve. To complete the analysis of the interaction between the shock wave and the compliant wall, we need to reconstruct the displacement of the latter as explained in §3.4. We briefly recall that the instantaneous displacement is the sum of a static component and a fluctuation. The static displacement, computed here using the spatial distribution of the wall-pressure for the rigid case, is shown in Fig. 12c, with the average position of the shock identified with the black line. This deformation is positive for $x < 0$, where the pressure on the upper surface is lower than on the bottom surface, and vice-versa for $x > 0$. The fluctuation is then modeled with the first three modes of the modal analysis vibrating at a frequency given by the experimental data (see Fig. 10). The amplitude of the three modes are then determined to best fit the experimental data shown in Fig. 12d. As shown in Tab. 2, the amplitude a_2 associated with the second mode of vibration is dominant compared to the first and third modes. Therefore, the pattern of the reconstructed fluctuation shown in Fig. 12d is very similar to that of the second mode. The sum of the static and fluctuation gives the reconstructed displacement of the compliant wall shown in Fig. 12b. We observe that the duration and amplitude of the negative displacement for $x > 0$ are longer and larger than for the positive displacement. The opposite pattern is found for $x < 0$. This is clearly the result of the existence of a the static deformation of the compliant wall caused by the pressure gradient imposed by the shock.

We now investigate the phase difference between the shock and wall oscillations by looking at Fig. 12d. An upward movement of the material upstream of the shock coincides with a downstream displacement of the shock and vice-versa. When the downstream part of the material presents an upward deformation, the shock position (solid black line) barely changes, presenting almost a plateau, as it is for the case between t_2 and t_3. This is consistent with the observation made in Fig. 11, where the shock seemed to remain in the same positions from t_2 till t_3. When looking at

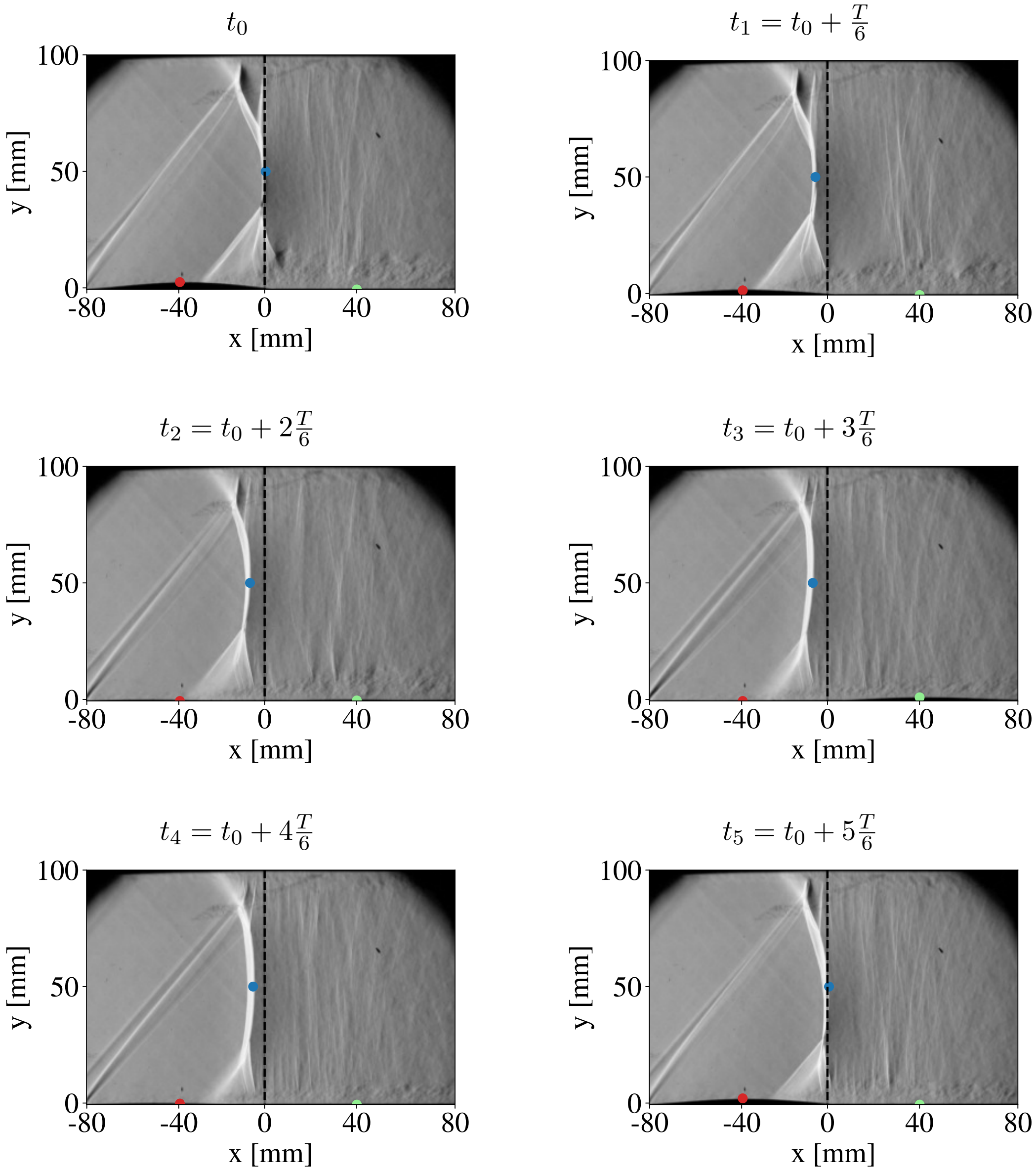

Figure 11: Instantaneous schlieren visualizations during an oscillation cycle of the compliant wall. Red, green and blue dots illustrate the displacement of the compliant wall and the shock.

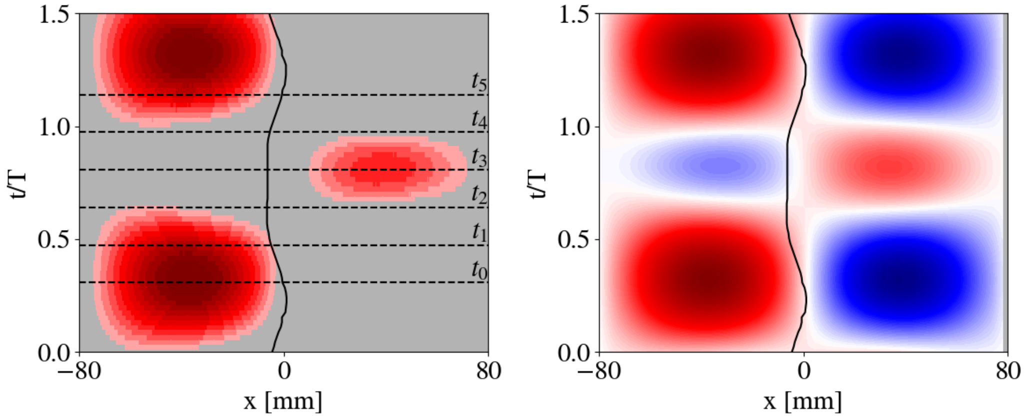

(a) Experimental data.

(b) Reconstructed data.

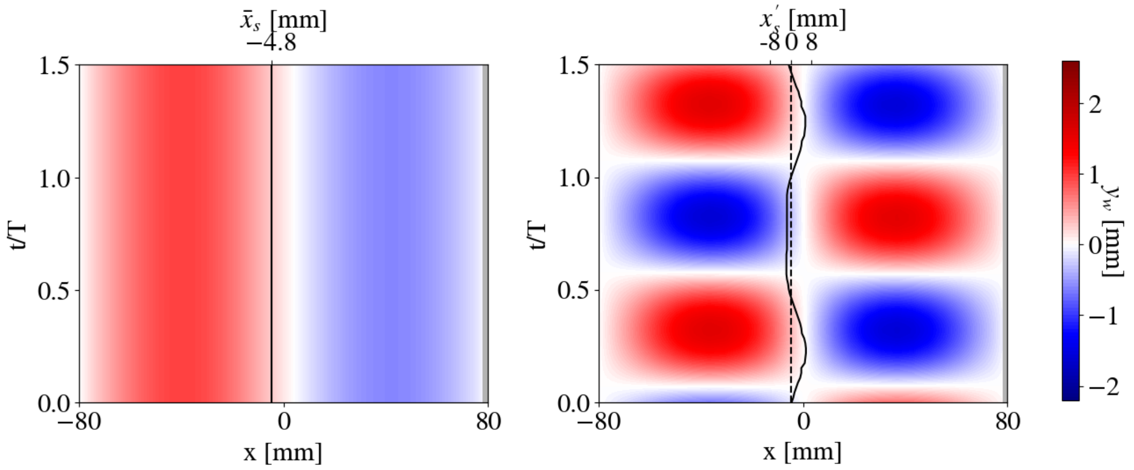

(c) Reconstructed static.

(d) Reconstructed fluctuation.

Figure 12: Spatio-temporal evolution of the compliant-wall displacement (color) and streamiwse shock position (black lines) (a) measured experimentally and (b) reconstructed by fitting a model. (c) Shows the reconstructed average displacement (color) and the average streamwise position of the shock (black line). Similarly, (d) reports the perturbation with respect to the time average of the wall displacement (color) and streamwise shock position (solid black line).

Fig. 12d, it is possible to see that the oscillation of the material presents a lag with respect to that of the shock. This implies that the most downstream position of the shock happens before the material has reached its maximum deformation. In order to assess the lag, the cross spectral density of both signals was computed. The phase between both wall displacement signals and the shock signals is 28°.

Regime of small-amplitude synchronized interaction This regime of interaction is characterized by periodic synchronized oscillations of the wall and the shock, whose amplitude is smaller than the static deformation of the wall. The particularities of this regime are illustrated by analyzing the interaction in shock configurations 1 and 6 (Tab. 1).

The dynamics for both shock configurations were analyzed by computing the spectrum with the Welch method for both the shock and wall displacement. For the wall, the spectrum was computed using the displacement signal at $x_{sensor} = 27$ mm retrieved from the displacement sensor as the schlieren does not provide enough resolution to capture the reduced wall oscillations. With respect to the flow, the spectrum was calculated with shock displacement at the center of the channel. The resulting spectra for both shock configurations are shown in Fig. 13

For shock configuration 1, the wall spectrum (Fig.13a, red) displays several peaks. The first three peaks, f_1, f_2, and f_3, are located at 119 Hz, 149 Hz and 205 Hz (dashed lines) respectively. Out of the three, f_1 is the dominant one. The spectrum of the flow (Fig.13a, blue), is characterized by a dominant peak at a frequency 119 Hz (first dashed line). This suggests that the shock presents a periodic oscillation at the first vibration frequency of the structure. Nonetheless, note that with respect to the regime of large-amplitude synchronized interaction (Fig. 10b), the magnitude of the shock oscillations is three orders of magnitude smaller. Therefore, the motion of the shock and the compliant wall is synchronized at f_1 with small amplitude oscillations.

In shock configuration 6, the wall spectrum displays a dominant peak f_1 at 122 Hz (Fig.13b, red). The two next peaks, f_2 and f_3 are located at frequencies 153 Hz and 209 Hz. On the flow spectrum however, the dominant peak appears at 209 Hz (third dashed line), which coincides with the third vibration frequency of the wall (Fig.13b, blue). This suggests that the shock oscillates at the structure's third vibration frequency. Seeing this result, one would expect a dominant peak at f_3, 209 Hz, on the compliant wall spectrum instead of at f_1, 122 Hz. The explanation for this discrepancy lies on the location of the displacement sensor with respect to the nodes of the third vibration mode (Fig. 8c). Being one of the two nodes located at $x = 27$ mm, the displacement sensor, which measures the wall motion at $x_{sensor} = 27$ mm, cannot see any contribution of the third mode to the wall motion, and thus its amplitude on the spectrum is small. In §3.4 the reconstructed data shows that the modal amplitude a_3, representative of the contribution of the third mode to the total motion of the compliant wall, is the largest, indicating that the compliant wall is mostly oscillating at its third vibration frequency. Consequently, this suggests that the shock and the compliant wall present a synchronized motion at structure's third vibration frequency, f_3. As in configuration 1, the amplitude of the shock oscillations is three orders of magnitude smaller than in the regime of large-amplitude synchronized interaction (Fig. 10b), meaning that the amplitude of the wall and shock motion is small.

Given the reduced amplitude of the oscillations, there are no major visible changes on the flow and the wall during one cycle. Thus, only one instantaneous schlieren visualization is used to illustrate the flow and wall for configurations 1 and 6 in Fig. 14a-b. On the first configuration, the shock topology resembles that of the rigid wall (Fig. 2a), except for the fact that the upper shock foot is smaller than the lower shock foot. In this case, no deformation is present in the schlieren, suggesting that there is a negative deformation. In configuration 6, the shock is inclined with a strong difference between the upper and lower foot. For this case, the wall presents a large upward deformation with a maximum around $x = -20$ mm. Nonetheless, from $x > 40$ mm no information of the deformation is available.

So as to complete the information on the wall's deformation obtained from the schlieren images, the static deformation of the compliant wall was computed assuming a Young modulus of 1.68 MPa. Fig. 14c-d presents the pressure difference

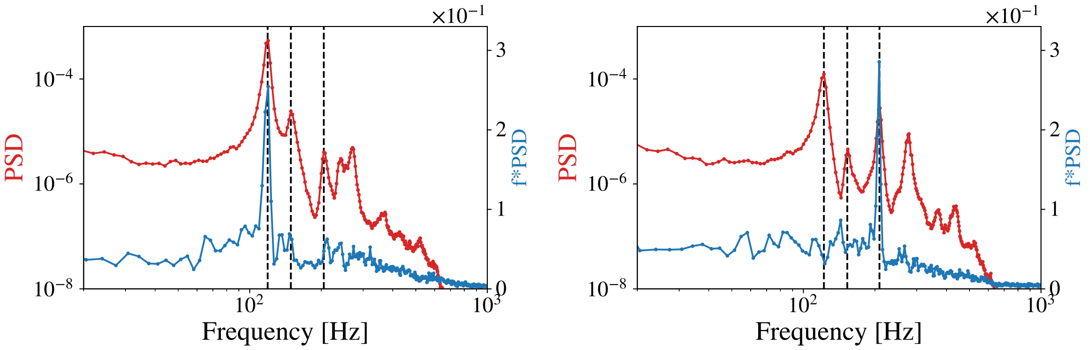

(a) Case 1 PSD wall displacement (b) Case 6 PSD wall displacement

Figure 13: Two regimes of small-amplitude synchronized interaction with large static deviation. (a) Case 1 for $\bar{x}_s = -45.1$ mm and (b) Case 6 for $\bar{x}_s = 41.1$ mm. In red the spectra of the compliant wall displacement measured with the displacement sensor at $x_{sensor} = 27$ mm. In blue the premultiplied spectra of the shock displacement. Note that it is three orders of magnitude smaller than in (Fig. 10b). The three dashed lines correspond to the first three vibration frequencies of the structure

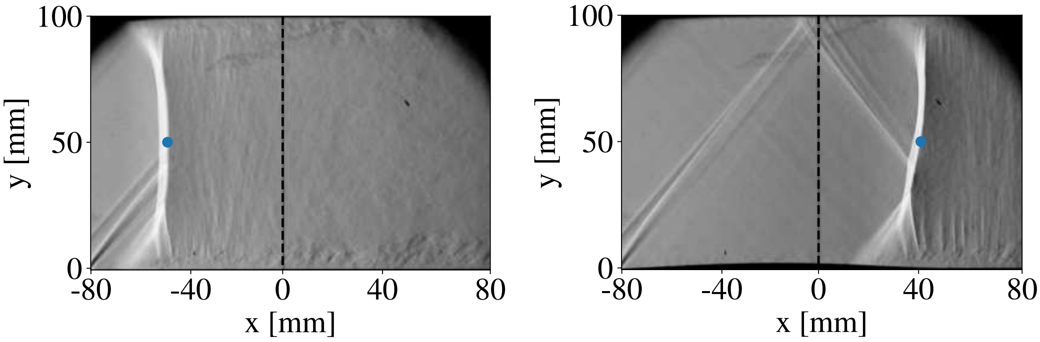

(a) Case 1 Instantaneous schlieren images (b) Case 6 Instantaneous schlieren images

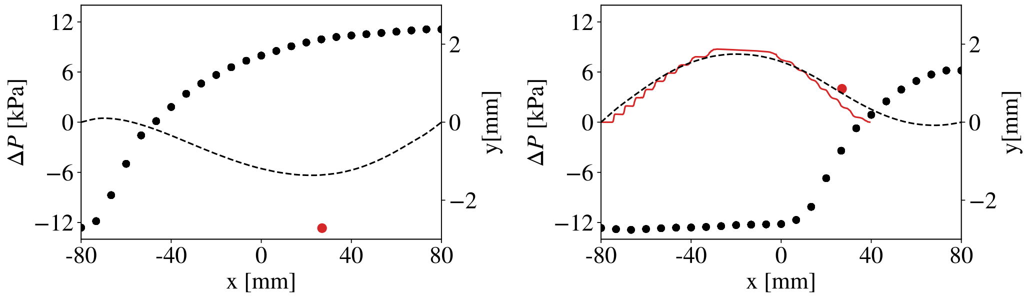

(c) Case 1 Pressure difference (d) Case 6 Pressure difference

Figure 14: Two regimes of small-amplitude synchronized interaction with large static deviation. (a,c) Case 1 for $\bar{x}_s = -45.1$ mm and (b,d) Case 6 for $\bar{x}_s = 41.1$ mm. (a-b) Instantaneous schlieren images. (c-d) Wall-pressure difference, $\Delta P(x) = P(x) - P_{bottom}$, as a function of x and deviation of the compliant wall computed with the linear elastic model (dashed curve), extracted from schlieren visualization (red curve) and obtained with the optical pointwise sensor (red dot).

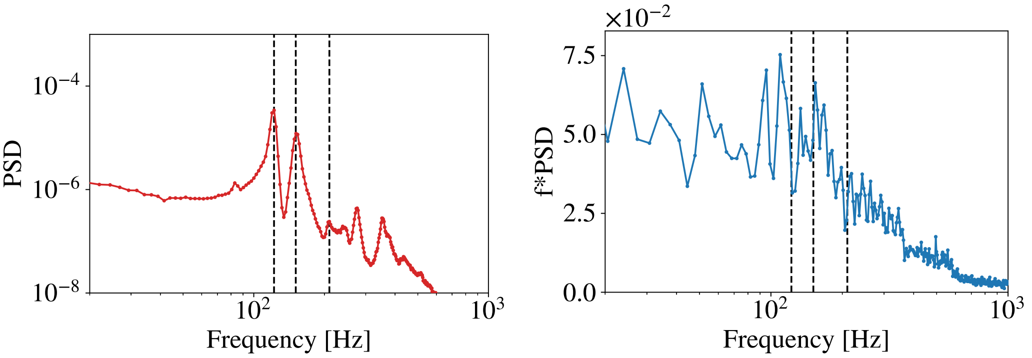

(a) PSD wall displacement

(b) f*PSD shock displacement

Figure 15: Regime of unsynchronized vibration, case 7 $\bar{x} = 73.9mm$. (a) Power spectrum density of the displacement of the wall obtained with the displacement sensor at $x = 27$ mm. (b) Premultiplied spectrum from the shock displacement signal obtained from the schlieren images. Note that the scale for $f * PSD$ is one order of magnitude smaller than in 13c-d.

distribution across the compliant wall, $\Delta P(x) = P(x) - P_{bottom}$, used on the computation. Fig. 14c-d shows as well the resulting static deformation with the average displacement value measured with the displacement sensor, and from the schlieren when available (red line).

For shock configuration 1, up to $x = -40$ mm, the low pressure from the supersonic region on the upper wall is lower than that of the cavity under the wall (Fig. 14c), which causes a negative pressure difference that results in an upward deformation of the compliant wall (Fig. 14c, dashed). Downstream this point, the situation reverses as the upper surface of the compliant wall is in contact with the higher pressure values of the subsonic region downstream of the shock, causing a positive pressure difference and a downstream deformation of the wall (Fig. 14c). In this configuration, there is no information from the schlieren visualizations but there is from the displacement sensor. Although the values do not coincide, the displacement sensor measures a negative displacement (Fig. 14c, red dot).

In shock configuration 6, up to $x = 40$ mm, the upper surface of the compliant wall is in contact with the low pressure coming from the supersonic flow. As this is lower than the pressure in the cavity, the pressure difference is negative causing an upward deformation of the compliant wall (Fig. 14d). The situation reverses downstream $x = 40$ mm, where the compliant wall presents a small downward deformation. In Fig. 14d, although there are some differences, both the average wall deformation from the schlieren images (red) and the displacement sensor (red dot) are in agreement with the computed static deformation (black dashed line).

Regime of Unsynchronized interaction This regime, illustrated by shock configuration 7 (Tab. 1), is characterized by small oscillations of the compliant wall and the shock which are not synchronized.

The dynamics of the interaction are illustrated through the spectrum of the compliant wall displacement obtained from the displacement sensor as well as the spectrum of the shock displacement at the center of the channel (Fig. 15a-b). The spectrum from the compliant wall presents a dominant peak at 122 Hz, f_1, with the second,

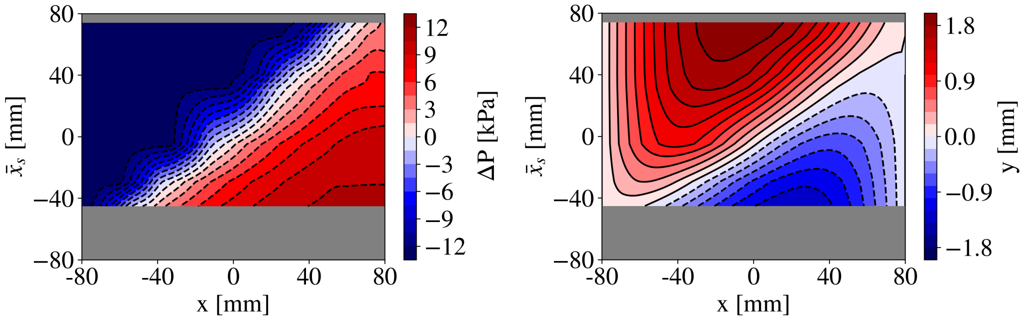

(a) Pressure wall difference

(b) Reconstructed static deformation

Figure 16: Isocontours of the (a) wall-pressure difference and (b) reconstructed static deformation of the compliant-wall as a function of the streamwise position x for several position $\bar{x}_s$ of the shock.

f_2, and third, f_3, peaks located at 151 Hz, and 210 Hz respectively (dashed lines). When looking at the spectrum of the flow, this presents a low frequency broadband bump, similar to the one obtained in the rigid case Fig. 3b. Thus, the flow excites the compliant wall but the flow does not lock-in to any of its vibration frequencies, contrary to the previous exposed regimes. Additionally, the amplitude of the shock oscillations is four orders of magnitude smaller than the one found in the synchronized large-amplitude regime, and one order of magnitude smaller than in the synchronized small-amplitude regime.

Regarding the topology of the flow as well as the deformation of the compliant wall caused by the pressure gradient imposed by the shock, it resembles that of configuration 6, explained in §3.5. Therefore, it is interesting that despite having similar flow and static deformations of the compliant wall, the behaviour of the interaction in both configurations is completely different.

Summary Having presented the three different regimes of interaction, this section aims at analyzing the influence the shock position along the wall has on the dynamics of the interaction as well as on the deformation of the compliant wall.

In order to analyse the effect on the compliant wall deformation, the static deformation fitted to the experimental data is presented as a function of the shock position in Fig. 16b. Fig. 16a presents the wall pressure difference used for the computation. For the most upstream shock position, most of the compliant wall's upper surface is in contact with the high pressure associated with the subsonic regime downstream the shock. Therefore, the aerodynamic loading exerted on the wall is positive, causing a negative deformation. At this point, the compliant wall presents its maximum negative displacement. As the shock moves upstream, the region upstream the shock, in contact with the low pressure from the supersonic region, becomes larger. In this area, the compliant wall is subjected to a negative pressure difference causing a positive deformation. When the shock is close to the center, the regions with positive and negative deformations are of the same length. As the shock reaches its most downstream position, the compliant wall presents a positive displacement. It is at this point were the maximum positive displacement is found.

The influence of the shock location on the interaction dynamics is displayed in Fig.17.

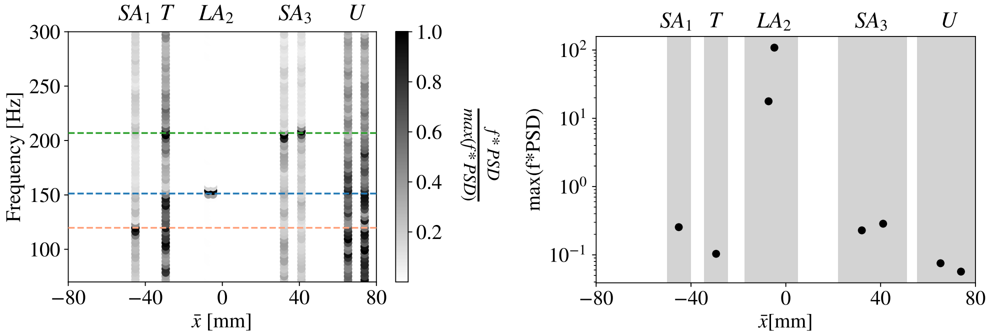

(a) Normalized f*PSD

(b) f*PSD maximum

Figure 17: (a) Normalized premultiplied spectrum of the shock displacement signal by the maximum amplitude between 20 - 1000 Hz as a function of the shock location. Horizontal dashed lines indicate the average values for the first vibration frequencies of the structure, f_1 (orange), f_2 (blue), and f_3 (green). (b) The maximum amplitude of the premultiplied spectrum of the shock oscillations used to normalized the premultiplied spectrum is presented in (a). SA stands for small amplitude, LA for large amplitude and U for unsynchronized and T for transition.

Fig.17a presents the normalized premultiplied spectrum of the shock displacement for the different shock locations along the wall displayed in Tab. 1. Its value has been normalized by the maximum amplitude on the premultiplied spectrum found between 20 Hz and 1000 Hz. Along side with the spectrum in Fig.17a, the average value of the vibration frequencies f_1 (orange), f_2 (blue) and f_3 (green), are reported. On the other hand, Fig. 17b shows the values used to normalized the premultiplied spectrum in Fig. 17a.

For the first configuration, the dynamics of the most upstream location, $\bar{x} = -45.1$ mm, corresponds to the synchronized small-amplitude regime (SA_1). At this location, the dominant peak matches the first vibration frequency of the structure (Fig. 17a, orange). As the shock moves downstream, in configuration 2, at $\bar{x} = -29.4$ mm, it undergoes a transition regime (T). At this point, the shock presents broadband oscillations as well as a peak coinciding with the third vibration frequency of the structure (Fig. 17a, green). When the shock is close to the middle of the compliant wall (locations 3 and 4, $\bar{x} = -7.3$ mm and $\bar{x} = -4.8$ mm respectively), it presents only one peak that coincides with the second vibration frequency of the structure (Fig. 17a, blue). Note that the amplitude of the oscillations for these configurations is at least two orders of magnitude higher than for SA_1 and T (Fig. 17b, blue). For this reason, these two locations are said to belong to the regime of synchronized large amplitude oscillations (LA_2). Further downstream, shock configurations 5 and 6, at locations $\bar{x} = 32.1$ mm and $\bar{x} = 41.1$ mm, present a dominant peak at the third vibration frequency of the structure (Fig. 17a, green). As the amplitude of the oscillations is smaller than for LA_2 (Fig. 17b), they are considered to be in the regime of the synchronized small amplitude vibrations (SA_3). At the two most downstream locations, configuration 7 and 8, positioned at $\bar{x} = 65.3$ mm and $\bar{x} = 73.9$ mm, they are unsynchronized (U) with the vibration frequencies of the structure (Fig. 17a) and present the smallest shock oscillations amplitudes (Fig. 17b, U).

From this last analysis it is clear that the shock location along the compliant wall has a paramount impact on the dynamics of the interaction. In order to find an explanation for this change in behavior, further analysis using the numerical tools should be conducted. For instance, it would be clarifying to retrieve the response of the compliant wall to an unsteady pressure field that could recreate the shock oscillations.

4. Conclusion

The interaction of a shock wave and a compliant wall has been experimentally characterized by means of schlieren visualization and a point displacement sensor. Due to the sparsity of the experimental data, a reconstruction method based on the three dimensional linear elastic equations is proposed to complete the experimental description of the interaction.

The effect of the shock location on the compliant wall deformation was assessed. It was found that due to the pressure gradient imposed by the shock, the compliant wall presents a downward deformation downstream of the shock and an upward deformation upstream of the shock. When the shock is located close to the compliant wall's leading edge, it presents only a downward deformation. As the shock moves downstream, an upward deformation appears upstream of the shock and the downward deformation downstream of the shock is reduced. When the shock is located at the trailing edge, the compliant wall presents only an upward deformation.

Throughout the experiments, three different regimes of interaction have been identified. The first one consists of large amplitude synchronized interactions of the shock and the compliant wall. A second regime of synchronized motion has also been identified, but with lesser amplitude oscillations. The last regime presented unsynchronized small oscillations of the shock and compliant wall. Whether one regime or another took place, highly depended on the position of the shock along the compliant wall. It was observed that for shock location close to the middle of the compliant wall, the interaction corresponded to the large-amplitude synchronized regime, where a lock-in of the shock motion to the second structure vibration frequency took place. For shock locations upstream of the middle, the interaction corresponded to the small-amplitude synchronized regime, presenting a lock-in of the shock motion to the first vibration frequency of the structure. For downstream shock positions, the small-amplitude synchronized regime was also found but the lock-in occurred with the third vibration frequency of the structure. When the shock was located at its most downstream positions, close to the trailing edge of the compliant wall, no lock-in of the shock motion to the structure vibration frequencies was found. In this stage, the shock presented low frequency broadband oscillations.

As to which is the cause for the existence of the three regimes of interaction, it is not clear to the authors. For a better understanding, the three dimensional linear elastic equation will be used to model the behaviour of the material and compute its response to an unsteady external forcing representative of the oscillatory motion of the shock. In this manner, it would be possible to discern if the observed lock-in at the different vibration frequencies of the structure is due to the excitation of a particular mode by the shock depending on its location with respect to the modal shapes.

Acknowledgements

This work is co-funded by the Direction Générale de l'Armement (AID Convention N° 2020 65 0022) and ONERA. The authors would like to express their gratitude to Julie Diani for granting them access to the rheometer at Laboratoire de Mécanique des Solides at École Polytechnique.

References

[1] K.R. Brouwer, R.A. Perez, T.J. Beberniss, S.M. Spottswood, and D.A. Ehrhardt. Experiments on a Thin Panel Excited by Turbulent Flow and Shock/Boundary-Layer Interactions. *AIAA Journal*, 59(7):2737–2752, 2021.

[2] P.J.K. Bruce and H. Babinsky. Unsteady shock wave dynamics. *Journal of Fluid Mechanics*, 603:463–473, 2008.

[3] R. Bur, R. Benay, A. Galli, and P. Berthouze. Experimental and numerical study of forced shock-wave oscillations in a transonic channel. *Aerospace Science and Technology*, 10(4):265–278, 2006.

[4] R. Bur, B. Corbel, and J. Delery. Study of passive control in a transonic shock wave/boundary-layer interaction. *AIAA Journal*, 36(3):394–400, 1998.

[5] N.T. Clemens and V. Narayanaswamy. Low-frequency unsteadiness of shock wave/turbulent boundary layer interactions. *Annual Review of Fluid Mechanics*, 46:469–492, 2014.

[6] D. Daub, S. Willems, and A. Gülhan. Experiments on aerothermoelastic fluid–structure interaction in hypersonic flow. *Journal of Sound and Vibration*, 531:116714, 2022.

[7] P. Dupont, C. Haddad, J.P. Ardissone, and J.F. Debiève. Space and time organisation of a shock wave/turbulent boundary layer interaction. *Aerospace Science and Technology*, 9(7):561–572, oct 2005.

[8] A. D'Aguanno, P. Quesada Allerhand, F. F. J. Schrijer, and B. W. van Oudheusden. Characterization of shock-induced panel flutter with simultaneous use of DIC and PIV. *Experiments in Fluids*, 64(15), 2023.

[9] M.A. Eitner, Y.-J. Ahn, L. Vanstone, M.N. Musta, J. Sirohi, and N.T. Clemens. Effect of Shock-Wave Boundary Layer Interaction on Vibratory Response of Compliant Panel. *AIAA SciTech Forum 2021*, pages 1–18, 2021.

[10] M.E. Erengil and D.S. Dolling. Unsteady wave structure near separation in a Mach 5 compression rampinteraction. *AIAA Journal*, 29(5):728–735, 1991.

[11] N. Gomez-Vega, M. Gramola, and P. J.K. Bruce. Oblique shock control with steady flexible panels. *AIAA Journal*, 58(5):2109–2121.

[12] M. Gramola, P. J.K. Bruce, and M. Santer. Off-design performance of 2D adaptive shock control bumps. *Journal of Fluids and Structures*, 93:102856, 2020.

[13] M. Gramola, P.J.K. Bruce, and M. Santer. Experimental FSI study of adaptive shock control bumps. *Journal of Fluids and Structures*, 81:361–377, 2018.

[14] F. Hecht. New development in freefem++. *J. Numer. Math.*, 20(3-4):251–265, 2012.

[15] E. Jinks, P. Bruce, and M. Santer. Wind tunnel experiments with flexible plates in transonic flow. *54th AIAA Aerospace Sciences Meeting*, pages 1–18, 2016.

[16] G.H. Jordan, N.J. McLeod, and L.D. Guy. Structural Dynamic Experiences of the X-15 Airplane, Tech. Rep. TN D-1158,. Technical report, NASA, Flight Research Center, Edwards, Ca., 1962.

[17] C. Riveiro Moreno, M. Couliou, N. Fabbiane, O. Marquet, and R. Bur. Interaction of shock-waves with a compliant wall. In *AERO 2023 - 57th 3AF International Conference on Applied Aerodynamics*, Bordeaux, France, March 2023. 3AF.

[18] F. Sartor, C. Mettot, R. Bur, and D. Sipp. Unsteadiness in transonic shock-wave/boundary-layer interactions: experimental investigation and global stability analysis. *Journal of Fluid Mechanics*, 781:550–577, 2015.

[19] S. Michael Spottswood, Timothy J. Beberniss, Thomas G. Eason, Ricardo A. Perez, Jeffrey M. Donbar, David A. Ehrhardt, and Zachary B. Riley. Exploring the response of a thin, flexible panel to shock-turbulent boundary-layer interactions. *Journal of Sound and Vibration*, 443:74–89, 2019.

[20] S. S. Tan, M. Gramola, and P. J.K. Bruce. Oblique shockwave boundary layer interaction on a flexible surface. *AIAA Scitech 2019 Forum*, pages 1–15, 2019.

[21] A. Tripathi, J. Gustavsson, K. Shoele, and R. Kumar. Response of a compliant panel to shock boundary layer interaction at mach 2. *AIAA Scitech 2021 Forum*, pages 1–15, 2021.

Appendix

A. Numerical modelling and discretization of the compliant structure

The three-dimensional instantaneous displacement $\boldsymbol{\xi}_s(\mathbf{x},t)$ of the polyurethane inserted in the aluminum container is modelled with the linear elasticity equations formulated as

$$\rho_s \partial_{tt} \boldsymbol{\xi}_s = \boldsymbol{\nabla} p_s + \mu_s \boldsymbol{\nabla} \cdot \left(\boldsymbol{\nabla} \boldsymbol{\xi}_s + \boldsymbol{\nabla} \boldsymbol{\xi}_s^T \right) \quad , \quad \lambda_s \, \boldsymbol{\nabla} \cdot \boldsymbol{\xi}_s = p_s \tag{9}$$

where the second equation defines the instantaneous solid pressure $p_s(\mathbf{x},t)$. These equations are satisfied in the domain Ω_s that is a parallelepiped with rectangular faces extending as $-80mm \le x \le 80mm$ in the streamwise direction, $-42.5mm \le z \le 42.5mm$ in the spanwise direction and $-L_y \le y \le 0$ in the vertical direction. The top surface ($y = 0$) corresponds to the interface with the high-speed flow in the test section of the wind tunnel. We recall that the Lame coefficients $\lambda_s = (E\nu_s)/(1+\nu_s)/(1-2\nu_s)$ and $\mu_s = 0.5E/(1+\nu_s)$ λ_s and μ_s are defined as a function of the Young modulus E and Poisson coefficient ν_s.

The static displacement $\boldsymbol{\Xi}_s(\mathbf{x})$ and pressure $P_s(\mathbf{x})$ of the structure are obtained by solving

$$\boldsymbol{\nabla} P_s + \mu_s \boldsymbol{\nabla} \cdot \left(\boldsymbol{\nabla} \boldsymbol{\Xi}_s + \boldsymbol{\nabla} \boldsymbol{\Xi}_s^T \right) = \mathbf{0} \quad , \quad \lambda_s \, \boldsymbol{\nabla} \cdot \boldsymbol{\Xi}_s = P_s \tag{10}$$

with appropriate conditions on the boundaries $\partial\Omega_s$ of the domain. At the four lateral boundaries with the aluminum container ($x = \pm 80$mm and $z = \pm 42.5$mm), Dirichlet boundary conditions are applied on the displacement, i.e. $\boldsymbol{\Xi}_s = \mathbf{0}$. At the top ($y = 0$) and bottom ($y = -L_y$) boundaries, Dirichlet boundary conditions are applied for the static pressure. For the bottom boundary that is the interface with still air, we impose $P_s(x, y = -L_y, z) = P_{meas}$ where $P_{meas} = 45$ kPa is the constant pressure measured with a static probe under the compliant structure during the experiments. For the top surface, we impose

$$P_s(x, y = 0, z) = P_f(x, y = 0, z) \tag{11}$$

where P_f is the static aerodynamic pressure. Note that it is partially determined in the experiments for the rigid wall configuration since it is measured at some streamwise positions in the symmetry plane $z = 0$ of the test section. The two-dimensional aerodynamic

Mesh size		Dynamic analysis		Static analysis	
$n_x \times n_y \times n_z$	n_{el}	f_n^1 [Hz]	Δf_n^1	ξ_z^{max} [mm]	$\Delta \xi_z^{max}$
$12 \times 9 \times 3$	1944	105.8	+1.5 %	1.013	−5.8 %
$16 \times 12 \times 4$	4608	104.9	+0.7 %	1.059	−1.5 %
$\mathbf{24 \times 18 \times 6}$	**15552**	**104.3**	–	**1.075**	–
$32 \times 24 \times 8$	36864	104.0	−0.3 %	1.081	+0.6 %
$48 \times 36 \times 12$	124416	103.7	−0.5 %	1.087	+1.1 %

Table 3: Mesh convergence study. The size of the mesh is represented by the number of elements along the x, y, and z directions, as well as by the total number of elements (n_{el}). Results from both dynamic and static analyses are monitored: the first natural frequency (f_n^1) and the maximum static displacement along the z direction (ξ_z^{max}) for the nominal shock configuration. The relative variation with respect to the results for the reference mesh (bold) is also reported.

pressure P_f is thus retrieved by a linear interpolation of the experimental measurements in the symmetry plane and a constant extrapolation in the spanwise (z) direction.

The unsteady displacement $\boldsymbol{\xi}'_s$ and pressure p'_s of the structure can be analyzed by assuming a modal decomposition as

$$\boldsymbol{\xi}'_s(\mathbf{x}, t) = \boldsymbol{\xi}_n(\mathbf{x})\, e^{\mathrm{i}\omega_\mathrm{n} \mathrm{t}} + \text{c.c.} \tag{12}$$

where ω_n is the (real) natural vibration frequency associated to the modal shape $\boldsymbol{\xi}_n$. Injecting the above modal decomposition in (9) gives the eigenvalue problem

$$\rho_s \omega_n^2 \boldsymbol{\xi}_n = -\boldsymbol{\nabla} p_n - \mu_s \boldsymbol{\nabla} \cdot \left(\boldsymbol{\nabla} \boldsymbol{\xi}_n + \boldsymbol{\nabla} \boldsymbol{\xi}_n^T \right) \quad , \quad 0 \quad = \quad -\lambda_s \, \boldsymbol{\nabla} \cdot \boldsymbol{\xi}_n + p_n \tag{13}$$

where the eigenvalues correspond to the square of the natural vibration frequencies ω_n^2 and the eigenvectors are the corresponding modal shape. Similar Dirichlet conditions are applied on the lateral boundaries while stress-free conditions are applied on the top and bottom boundaries.

The static elasticity equation (10) and the eigenvalue problem (13) are discretized using a standard finite-element method. The open-source library FreeFEM [14] is used to assemble the sparse matrices. The numerical interface with the open-source library MUMPS is used to perform sparse-LU factorization/inversion of these matrices. The interface with the open-source library ARPACK is used to determine the eigenvalues and eigenvectors.
In order to determine a suitable discretization of the domain, a convergence study was conducted. The number of elements along the three directions – n_x, n_y, and n_z – has been varied and results from both dynamic and static analyses have been monitored. Second-order langrangian elements are used for the displacement, while first order ones are for the pressure field. Tab. 3 presents the evolution of the prediction of the first natural frequency with the mesh spatial resolution, as well as of the maximum static deformation for the nominal shock configuration. The reference configuration – $n_x = 24$, $n_y = 18$, and $n_z = 6$ – was chosen as it is a good compromise between computation time and spatial resolution. An example of the static deformation computed for configuration 4 computed with the corrected Young modulus — as it is explained in §3.3 – can be found in Fig. 18 as well as the reference mesh.

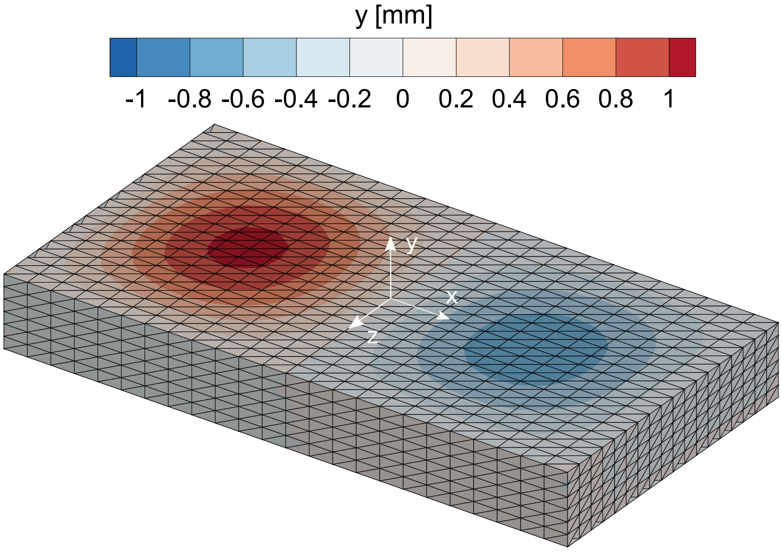

Figure 18: Typical mesh and isocontours of the static deformation computed for the nominal shock configuration.